AIAA JOURNAL
Vol. 40, No. 8, August 2002

Microfabricated Shear-Stress Sensors, Part 3: Reducing Calibration Uncertainty

Mehul P. Patel,* Eli Reshotko,† and Daniel Hyman‡
Case Western Reserve University, Cleveland, Ohio 44106

A calibration procedure for wall shear-stress sensors based on continuum isothermal compressible flow has been developed. Microfabricated electromechanical floating element sensors for direct measurement of wall shear stress are chosen for calibration. The calibration equation states a linear relation between the channel height and the calibrated shear stress, resulting in an overall calibration uncertainty as a result of inaccuracy in the channel height measurement. A novel microstrip technique using basic principles of microwave engineering is used to measure the channel height with a high degree of accuracy. The uncertainties involved in the measurement of all of the parameters that are related in any way to the calibration equation are identified, measured, evaluated, and integrated into the equation to obtain a complete error analysis of the calibration procedure. The calibration of shear-stress sensors is successfully completed with an overall accuracy of 2%.

I. Introduction

THE design and fabrication of microfabricated electromechanical (MEMS) wall shear-stress sensors investigated in this study are described in Ref. 1, followed by preliminary testing and calibration efforts described in Ref. 2. These sensors employ a direct measurement technique, using floating elements that displace against spring suspension systems when exposed to shear stress. Indirect measurement techniques work under assumptions that relate the shear stress to the quantities that are directly measured. Because there exists a direct correlation between the shear stress over the floating element area and the floating element deflection caused by the shear force, this technique qualifies as a direct measurement technique. This paper examines in detail the calibration issues discussed in Ref. 2.

Despite considerable work done on measurement of wall shear stress, there is still a need for an easily implemented and reliable technique of direct measurement of wall shear stress.[3–6] The apparatus and calibration process used in Ref. 2 introduced a number of uncertainties in device measurement including limitations in instrument accuracy or operator-dependent uncertainties. During previous work, preliminary calibration of these sensors was done to an estimated 5% calibration accuracy.[7] The uncertainty involved in the optical measurement of channel height at the location of the sensor was calculated to be $\pm 20\ \mu$m as a result of operator-dependent and instrument-dependent uncertainties. Other errors originated from curve fits for the pressure gradient and the process of positioning of the sensor die flush to the channel. Micromachining techniques as described in Ref. 8 are used to manufacture the sensors used in this work in order to eliminate accuracy limitation dependent on sensor fabrication. A picture of a typical MEMS based shear-stress sensor is shown in Fig. 1. This paper describes the effort to refine the development of the wall shear-stress calibration system and increase the overall calibration accuracy.

Received 15 July 2001; revision received 4 March 2002; accepted for publication 11 March 2002.

*Graduate Research Assistant, Department of Mechanical and Aerospace Engineering; currently Senior Aerodynamicist, Orbital Research, Inc., 673 G Alpha Drive, Cleveland, OH 44143. Member AIAA.

†Kent H. Smith Professor Emeritus of Engineering, Department of Mechanical and Aerospace Engineering. Fellow AIAA.

‡Graduate Research Assistant, Department of Electrical Engineering and Computer Science, and Hughes Fellow, Hughes Research Laboratories; currently President, XCom Wireless, Inc., 1718 E. Ocean Boulevard, Suite 4, Long Beach, CA 90802.

II. Theoretical Analysis

The schematic of a high-aspect-ratio (96–145) flow channel, which is used for sensor calibration, is shown in Fig. 2. The flow inside the continuum flow channel is approximated to be a two-dimensional flow. A steady continuous flow of nitrogen gas is supplied from a regulated nitrogen tank. It is assumed, for the channel with uniform cross-sectional area, that the pressure variation is only along the flow direction. The momentum theorem of fluid mechanics is used to derive the relation that is used for calibrating these shear-stress sensors. Because the calibration relation is derived from a momentum balance across the flow channel, it is independent of whether the flow is laminar, transitional or turbulent. Assumptions for the fluid flow are as follows: 1) the flow is steady; 2) the local velocity or Mach number distributions can be represented by their mean values across the channel height; and 3) the temperature is constant.

A control volume, defined as an imaginary fixed volume inside the flow channel through which a fluid may flow, is schematically illustrated in Fig. 3. The pressure gradient inside the flow channel is the driving force of the fluid.

A. Continuity Equation

The continuity equation states that

$$\rho AV = \text{constant} \tag{1}$$

For an ideal gas $p = \rho RT$, and $V = Ma$, where $a = \sqrt{(\gamma RT)}$. Therefore, Eq. (1) implies

$$(p/RT)AM\sqrt{\gamma RT} = \text{constant} \tag{2}$$

Because cross-sectional area is constant and gas is assumed to be isothermal, the differential form of Eq. (2) becomes

$$\mathrm{d}M^2 = -2M^2\frac{\mathrm{d}p}{p} \tag{3}$$

B. Momentum Balance

Applying momentum balance on a rigid control volume of height b, width w, and differential length $\mathrm{d}x$ yields

$$[\rho V^2 \times b \times w]_{x+\mathrm{d}x} - [\rho V^2 \times b \times w]_x$$

$$= [p \times b \times w - (p + \mathrm{d}p) \times b \times w] - 2\tau_w w\,\mathrm{d}x$$

where τ_w is the wall shear stress and is

$$\tau_w = -\frac{b}{2}\left[\frac{\mathrm{d}p}{\mathrm{d}x} + \frac{\mathrm{d}}{\mathrm{d}x}(\rho V^2)\right] = -\frac{b}{2}\left[\frac{\mathrm{d}p}{\mathrm{d}x} + \frac{\mathrm{d}}{\mathrm{d}x}\left(\frac{p}{RT}M^2\gamma RT\right)\right]$$

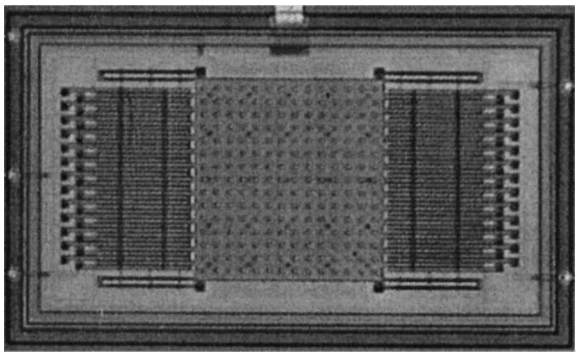

Fig. 1 CWRU/AMMI floating element shear-stress sensor.

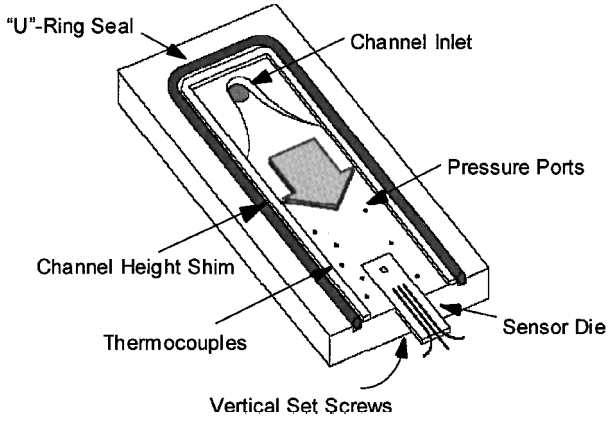

Fig. 2 Schematic of the flow channel.

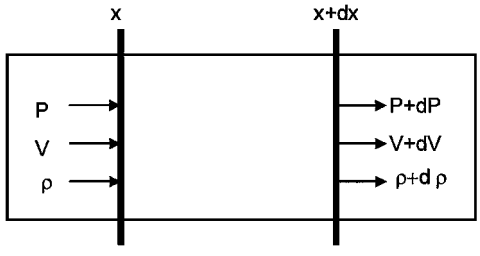

Fig. 3 Control volume of the flow channel.

or

$$\tau_w = -\frac{b}{2}\left[\frac{\mathrm{d}p}{\mathrm{d}x} + \gamma M^2 \frac{\mathrm{d}p}{\mathrm{d}x} + \gamma p \frac{\mathrm{d}M^2}{\mathrm{d}x}\right] \tag{4}$$

From Eq. (3)

$$\gamma p \frac{\mathrm{d}M^2}{\mathrm{d}x} = -2\gamma M^2 \frac{\mathrm{d}p}{\mathrm{d}x} \tag{5}$$

Substituting Eq. (5) in Eq. (4),

$$\tau_w = -\frac{b}{2}\left[\frac{\mathrm{d}p}{\mathrm{d}x}(1 - \gamma M^2)\right] \tag{6}$$

where τ_w is the wall shear stress and $\mathrm{d}p/\mathrm{d}x$ is the pressure gradient at the sensor location. The Mach number term in Eq. (6) incorporates the compressibility effect for an isothermal channel flow into the calibration equation. A similar model described in Refs. 9–11 was presented for the calibration of microfabricated shear-stress sensors but did not include the compressibility effect, which can affect the overall calibration accuracy.

There are other forces acting on the floating element, such as 1) the gauge force arising as a result of the pressure differential across the floating element and 2) a shear force arising from the flow underneath the floating element. The total force on the sensor element divided by the surface area of the element is the effective shear stress τ_{eff} given by

$$\tau_{\text{eff}} = -\frac{\mathrm{d}p}{\mathrm{d}x}\left|\frac{b}{2}(1 - \gamma M^2) + \frac{g}{2} + t\right| \tag{7}$$

Again, $(\mathrm{d}p/\mathrm{d}x)$ is the pressure gradient at the sensor location, b is the channel height, M is the Mach at the sensor location. Additionally, g is the gap spacing between the floating element and the fixed substrate, and t is the thickness of the floating element.

III. Measurement of Parameters for Sensor Calibration

From the calibration relation stated in Eq. (7), the parameters that need to be measured experimentally for determining the shear stress at the sensor location are as follows: 1) channel height b, as defined by the thin shim thickness; 2) pressure gradient $(\mathrm{d}p/\mathrm{d}x)$, at the sensor location; 3) Mach number M at the sensor location; 4) thickness t of the floating element; and 5) the gap g between the floating element and the electrostatic shield next.

A. Channel Height

The calibration equation (7) states a linear relation between the channel height b and the calibrated shear stress, resulting in an overall calibration uncertainty caused by measurement inaccuracy of the channel height. Previous calibration efforts described in Refs. 2 and 7 used optical microscopes for the measurement of channel height, leading to an overall inaccuracy of 5%. The primary disadvantages of optical stage measurement methods are lack of precision and difficulty of an in situ measurement.

In the present work a novel microstrip technique is designed from the fundamental principles of microwave engineering and is demonstrated to reduce the uncertainty in the measurement of channel height to 1.5%. The following subsections illustrate the design and implementation of this novel microwave technique for the channel height measurement.

1. Microstrips

Microstrip lines are thin planar transmission lines, which support quasitransverse electromagnetic waves at microwave frequencies.[12] These lines are fabricated by photolithographic processes, in which conductive materials such as gold or copper are deposited on a dielectric substrate having a ground plane. The geometry of a typical microstrip line is shown in Fig. 4. A conductor of width w is printed on a thin, grounded dielectric substrate of thickness d and relative permittivity ε_r. A sketch of the field lines is shown in Fig. 5.

Using a quasistatic approach, the phase velocity v_p and propagation constant β can be approximated as follows: phase velocity $v_p = c/\sqrt{\varepsilon_e}$, propagation constant $\beta = k_0\sqrt{\varepsilon_e}$, where $c = 3 \times 10^8$ m/s is the speed of light and ε_e is the effective dielectric constant of the microstrip line. For a loss-less line the characteristic impedance Z_0, which is the ratio of voltage to current for the traveling wave, is expressed as $Z_0 = \sqrt{L/C}$, where L and C are inductance and capacitance per unit length of the line. Given the substrate (air) thickness b (namely, the channel height) and conductor width w, the characteristic impedance of the line Z_0 is[12]

$$Z_0 = \frac{120\pi}{\sqrt{\varepsilon_e}[w/b + 1.393 + 0.667\,\ln(w/b + 1.444)]} \qquad \text{for} \quad w/b \geq 1 \tag{8}$$

The w/b ratio is given by

$$w/b = 2/\pi\left\{B - 1 - \ln(2B - 1) + (\varepsilon_e - 1)/2\varepsilon_e \times [\ln(B - 1) + 0.39 - 0.61/\varepsilon_e]\right\} \qquad \text{for} \quad w/b \geq 1 \tag{9}$$

where

$$B = 377\pi \Big/ 2Z_0\sqrt{\varepsilon_e}$$

The only significant assumption for the use of these microstrip analysis equations is that the channel height is constant along the

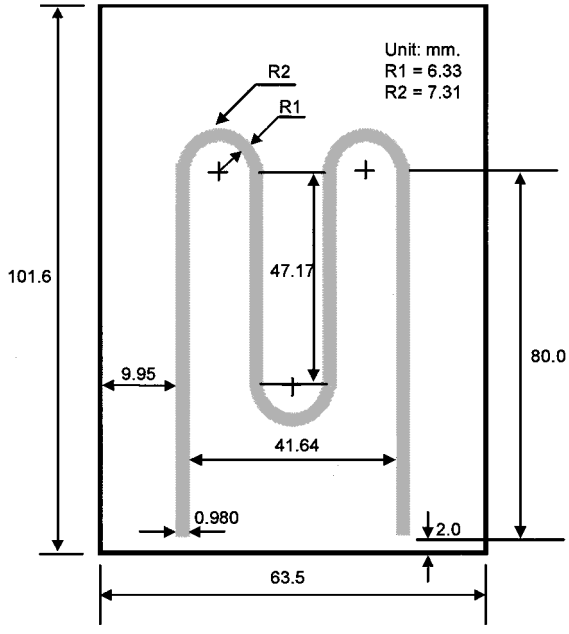

Fig. 4 Design of the gold transmission line (microstrip).

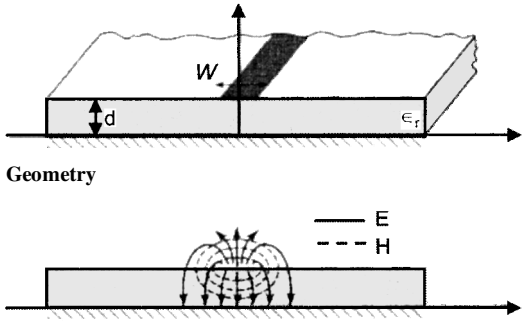

Fig. 5 Microstrip transmission line.

length of the microstrip line. Variance in channel height would provide variance in characteristic impedance along the line. The input reflections caused by this variance will be measurable in terms of phase and amplitude variations and will be readily identifiable in measurements should variance be present.

2. Design of the Gold Line

A gold line of width w and overall length l, as shown in Fig. 4, is deposited on the lower surface of the glass cover plate by a shadow mask process.[13,14] The shim that separates the glass cover plate from the steel base plate defines the channel height b. The medium between the plates is air. The effective dielectric constant of air ε_e is 1. If the characteristic impedance Z_0 and width w are known, the distance b can be calculated from Eqs. (8) and (9).

In the present design microwave power from a source inside the Network Analyzer HP4395A is launched onto the microstrip line. The characteristic impedance of the transmission line is designed to be approximately 50 Ω. The purpose of designing the characteristic impedance to 50 Ω is to closely match the source impedance, minimizing reflected waves upon launch. A block diagram of the set up for the channel height measurement is shown in Fig. 6.

The characteristic impedance of the microstrip transmission line is extremely sensitive to the separation distance (channel height), where the line width of channel height defines the impedance of the line. The channel base is treated as an infinite conducting plane some distance away from the transmission line. So by measuring the reflection and the transmission effects, the separating channel height can be determined. The value of effective dielectric constant ε_e, which is 1, and the characteristic impedance Z_0 that is preset

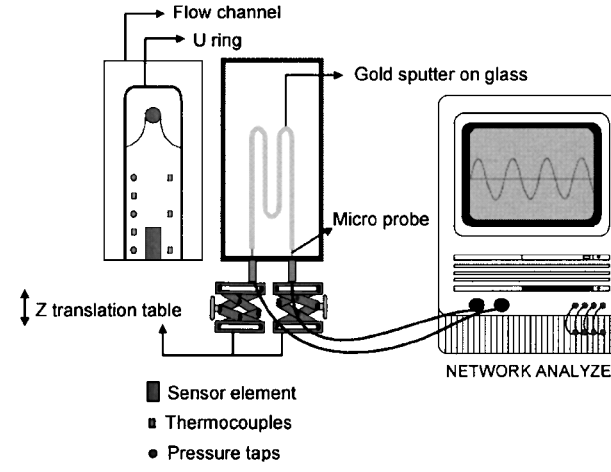

Fig. 6 Channel height measurement setup using HP4395A network analyzer.

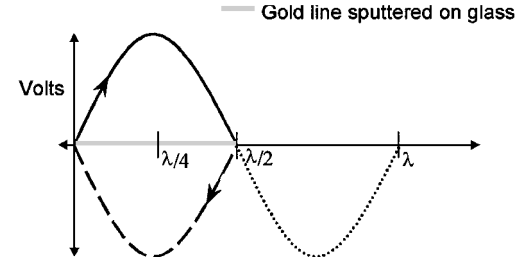

Fig. 7 Length of the transmission line (material: gold).

at 50 Ω are substituted in Eqs. (8) and (9) keeping a fixed channel height b, say, 200 μm. The w/b ratio is 4.9 for the given values of Z_0 and b. The width of the gold line w obtained from the w/b ratio is 983 μm. Length of the gold line is also an important parameter to identify because the reflection coefficient as a function of frequency depends heavily on feature length.

It is desired to first identify the frequency at which one obtains a zero value for the reflection coefficient, which is possible only in the special case where the total signal that is transmitted is completely reflected by 180 deg out of phase. When the length of the line is $\lambda/2$, the reflected wave is completely out of phase, and it cancels out the transmitted wave. A large value of return loss corresponds to a small-reflected signal just as a large value for insertion loss corresponds to a small-transmitted signal. A marker in HP4395A is used to identify the frequency at which the lowest reflection coefficient is obtained. The frequency sweep/magnify feature in HP4395A allows zooming in a particular range of operating frequencies to obtain a much closer look at the values of the reflection coefficient.

In examining Fig. 7, the length for complete reflection can be any value that satisfies the relation $l = \lambda/2 + n$, where n is a positive integer. The condition of obtaining a zero reflection coefficient $\Gamma = 0$ is satisfied for all values of l as far as it satisfies the given relation. The maximum length is fixed to $\lambda/2$ in this case because of the substrate size constraints from the gold sputtering machine; the maximum length of the glass that the machine can handle is 11.4 cm. The glass cover plate is separated into two pieces, with the piece containing the gold line at length 10.16 cm. The design of the gold line is shown in Fig. 4. The average length of the gold line is 32.12 cm, which is the mean length of the as-deposited inside and outside of the patterned line. The averaged length of the gold line is 32.12 cm, calculated by taking the mean length of the inside and outside edges of the line.

The operating frequency 466.867 MHz is obtained from the relation $c = \lambda f$, where $\lambda = 2l$. Because the range of the operating frequencies for the HP 4395A is 10 kHz–500 MHz, the acceptable wavelength λ must be greater than 600 mm. This is the reason for the curved shape of the gold line, rather than a straight line. The losses are minimum on a straight line. The higher the operating frequency,

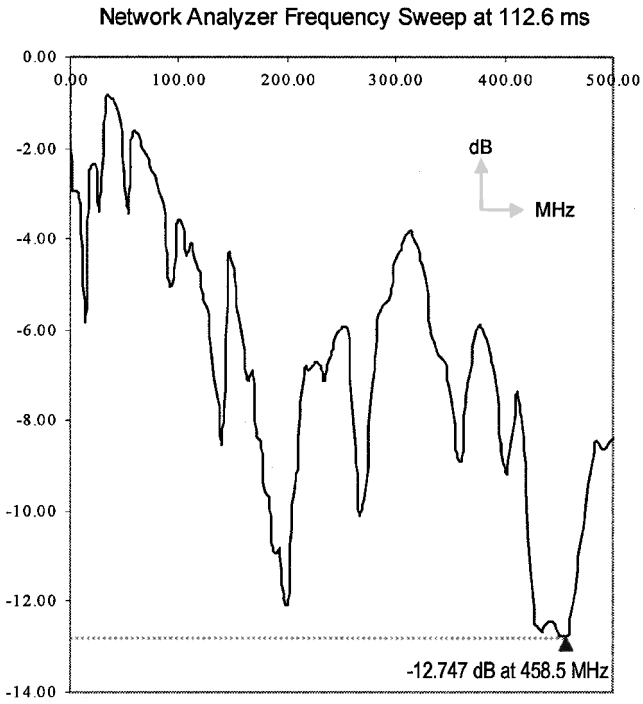

Fig. 8 Network Analyzer plot showing minimum Γ at 458.5 MHz.

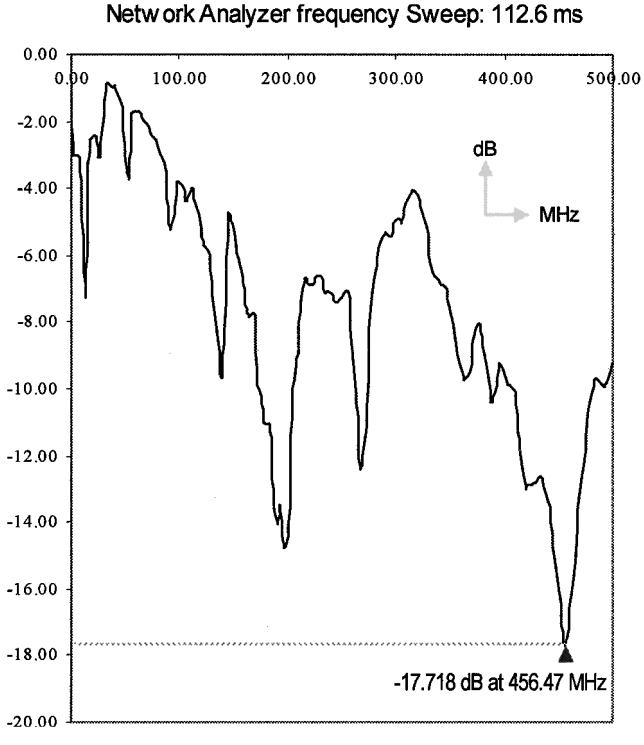

Fig. 9 Network Analyzer plot showing minimum Γ at 456.47 MHz.

the shorter the length of the transmission line and better the reflection characteristics. Figures 8 and 9 are the screen shots taken from the Network Analyzer HP4395A display screen showing a minimum reflection occurring at 458.5 and 456.5 MHz, respectively. The reflection coefficient of the transmission line for the given designed parameters should be equal to zero in an ideal case, but there are return losses for the following reasons:

1) The gold line as shown in Fig. 4 has three curves that contribute both phase-shifted return reflection of the signal as well as the launching of surface waves resulting in energy loss.

2) The launching of the coaxial from the HP 4395A to the gold line involves a mechanism, which forces a compression fit between the coaxial probe and the microstrip line. This method of connecting the coaxial and microstrip transmission lines mechanically damages the launch end of the line with each attempt to make a connection. Eight to 10 such attempts were required for successful connections to obtain a complete set of data for a particular channel height.

3) Interference of the wave propagation in the microstrip mode is caused by the partial metalization on the sensor located in front of the gold line, which is separated by a distance of channel height. The capacitance of the microstrip signal line to the sensor is small relative to the surrounding ground plane, so that a slight shunt inductance characteristic to the line would be present.

4) The width of the gold line is not constant throughout the entire length. There are variations in the width of the gold line along its entire length leading to reflection losses. This is because of a delineation accuracy limitation of the shadow mask gold sputtering process employed.

These factors contribute a variance to the nominal value of the reflection coefficient, and these uncertainties are observable in terms of measured return loss. The channel height is calculated based on the return loss, and so the uncertainty in return loss measurements corresponds directly to the uncertainty in the channel height measurement. The output from the Network Analyzer HP 4395A for the return losses is in decibels from which the values of Γ are calculated. Details of the theory and the equations that are used for obtaining the reflection coefficient Γ are described in Ref. 12. The estimate for the uncertainty in the measurement of channel height, after a complete uncertainty analysis, is ±1.5%. This channel height measurement uncertainty is estimated to be comparable to the fluctuation in channel height itself, so that attempts to further characterize higher levels of measurement precision are unlikely to improve the accuracy beyond this point.

B. Pressure Gradient

The negative pressure gradient $\mathrm{d}p/\mathrm{d}x$ along the flow path is characterized with the help of a National Institute of Standards and Technology (NIST)-calibrated pressure transducer OMEGA PX236, which is connected to five pressure taps. The pressure taps are evenly distributed inside the flow channel. The first and the fifth pressure taps are located at a distance of 38.735 and 8.25 mm from the channel end, respectively. A fixed distance of 7.625 mm is maintained between each of the taps. These taps enable direct measurement of the static pressures at these locations. A common switch is used to connect the pressure transducer to each of the five pressure taps, thus eliminating the need of more pressure sensors. Once the pressure readings are obtained, the dynamic property of the flow can be inferred from the plot of the pressure gradient. A fifth-order polynomial curve fit $p(x) = ax^4 + bx^3 + cx^2 + \mathrm{d}x + e$ is then made to these pressure data to obtain the pressure at the sensor location x. The pressure gradient $p'(x) = 4ax^3 + 3bx^2 + 2cx + \mathrm{d}$ at the sensor location x is obtained from interpolation of the curve. The estimated uncertainty of pressure gradient determination for the presented work is ±0.2%.

C. Mach Number

Mach number is determined by measuring the average fluid velocity at the sensor location V_{sensor}. V_{sensor}, a function of the volumetric flow rate Q_{sensor} and the cross-sectional area A of the fluid flow is given by $V_{\text{sensor}} = Q_{\text{sensor}}/A$. The flow rate Q_{sensor} at the sensor location is determined from the measurements taken upstream of the channel by a NIST-calibrated variable area flowmeter. The scale of the rotameter is calibrated on the assumption that its output is at atmospheric pressure, which here is actually subjected to a backpressure. To obtain the correct flow rate, a simple correction factor can be determined for differing backpressures.[15] Assuming isothermal flow, if pressure at the exit of the rotameter P_{rot} is measured, for a given flow rate reading Q_{rot} the flow rate at the sensor location Q_{sensor} is given by $Q_{\text{sensor}} = Q_{\text{rot}}\sqrt{(P_{\text{rot}}P_{\text{atm}})/P_{\text{sensor}}}$, where P_{sensor} is the pressure at the location of the sensor and P_{atm} is atmospheric pressure. The velocity at the sensor location is then measured by dividing the actual flow rate at the sensor location Q_{sensor} by the cross-sectional area through which the fluid flows, that is,

$V_{\text{sensor}} = Q_{\text{sensor}}/A$. Mach number is then determined by comparing the sensor velocity to the local speed of sound V_{sound} at the measured temperature. The Mach number where choking occurs for an isothermal flow of a perfect gas in a constant-area duct in the presence of wall friction is given by $1/\sqrt{\gamma}$ (Ref. 16).

D. Thickness and Gap Measurements

The values of the thickness of the floating element t and the gap between the floating element and the fixed substrate g are obtained from the actual design specifications of the floating element. The values of g and t are 0.0025 and 0.0020 mm, respectively. Even a 10% variation from design values of t and g contribute negligibly to the error in τ_w measurements.

E. Temperature Measurements

To ensure isothermal conditions inside the channel, continuous monitoring of the temperature at different locations inside the flow channel is necessary. Three tungsten wires acting as P-type thermocouples are inserted in $\frac{1}{16}$th-in.-diam holes at three different locations inside the channel bed. The locations of these probes are at distances of 8.25, 23.49, and 38.735 mm, respectively, from the channel end. The thermocouple tips are flush mounted to the inside of the channel. The thermocouple probes provide a real-time temperature measurement at all three locations without causing any obstruction to the fluid flow.

IV. Uncertainty Analysis

A square-root-of-the-sum-of-the-squares method, as described by in Ref. 17, is used for computing an absolute error of the uncertainties that are incorporated with the calibration. Relative weight of each measurement is taken into consideration as a linear operator based on its power relationship to the value. First, the fractional uncertainties of the individual variables that are used in Eq. (7) are measured. Then, the partial derivative of the equation is taken with respect to each component and divided by the total to obtain an equation for how the fractional uncertainties compound. The fractional uncertainty $\Delta\tau/\tau$, which is also defined as the fractional uncertainty of the calculated effective stress calculated from Eq. (7), is

$$\frac{\Delta\tau_{\text{eff}}}{\tau_{\text{eff}}} = \left[\sum\left(\frac{\partial\tau_{\text{eff}}}{\partial X_i}\Delta X_i\right)^2\right]$$

Applying the square-root-of-the-sum-of-the-squares rule to Eq. (7), the fractional uncertainties of the individual quantities can be obtained. Combining all individual uncertainties, we get the fractional uncertainty of the calculated effective shear stress:

$$\left(\frac{\Delta\tau_{\text{eff}}}{\tau_{\text{eff}}}\right)^2 = \left[\frac{\Delta(\partial p/\partial x)}{\partial p/\partial x}\right]^2 + \left(\frac{\Delta b}{b}\right)^2 + \left(\frac{2\gamma M\Delta M}{[1-\gamma M^2+g/b+2t/b]}\right)^2 + \left(\frac{(1/b)\Delta g}{[1-\gamma M^2+g/b+2t/b]}\right)^2 + \left(\frac{2\Delta t/b}{[1-\gamma M^2+g/b+2t/b]}\right)^2 \tag{10}$$

The terms inside the sets of parentheses are the fractional uncertainties of the individual quantities. A systematic approach to the identification and estimation of measuring system errors based on manufacturer's specifications is described in Ref. 18. The instruments used in the calibration process include pressure transducer, rotameter, Network Analyzer HP4395A, and multimeters.

The pressure transducer calibration was found to be very well within 1% accuracy as specified on the calibration sheet. The inaccuracies of the pressure sensor from the taps contribute in a nonlinear fashion because the gradient is the derivative of a line based on a measured distance. If the pressures for the curve fit were to be modified by +1% at the maximum and −1% at the minimum value, the pressure gradient at the location of the sensor changes less than 0.2%. Thus, maximum calculated $[\Delta(\partial p/\partial x)/(\partial p/\partial x)] = 0.002$.

Because of the tendency of the rotameter to drift during a constant flow, the volumetric flow rate varies and leads to uncertainty. This would lead to a slightly different pressure reading as a result of the varying flow rates, and the sensor output would not correlate to the recorded flow rate and pressure gradient. To ensure the flow-rate accuracy, two different rotameters, one with a lower range (288.0–7590.0 std ml/min) and the other with a higher range (1384.6–46132.7 std ml/min) are used, and the flow rates are tested for the same test conditions. Uncertainty contributed from this drift is typically on the order of 5–10%.

The relationship of the uncertainty in the Mach number factor to that of the total compressibility correction is obtained by taking the derivative of the correction factor. The compressibility correction is less than 0.1% at low shear stresses yielding the compressibility correction fractional uncertainty less than 0.1%. The maximum compressibility correction fractional uncertainty (∼0.5%) occurs at higher shear stresses (Mach 0.4). The inaccuracies in the channel height measurement and the pressure gradient measurements when reduced to the level comparable to that needed for 1% calibration accuracy, the uncertainty in the compressibility correction drops because of the dependence on channel height uncertainty in its calculation. Thus, the uncertainty in the compressibility correction factor can be neglected for any flowrate, any shim, and any reasonable accuracy limits of calibration. The fractional uncertainties of the underflow shear stresses are neglected following the same line of reasoning. The maximum uncertainty in the measurement of the Mach number ($\Delta M/M$) is 0.025.

Channel height measurements done using the new microstrip technique indicate a sensitivity of about ± 3 μm, which is about $\pm 1.5\%$ for a channel height of 200 μm. Also, the maximum uncertainty in the measurement of g, the gap spacing between the floating element and the fixed substrate ($\Delta g/g$) and t, the thickness of the floating element ($\Delta t/t$) is 0.1. These had negligible effect on overall error: $[\Delta(\partial p/\partial x)/(\partial p/\partial x] = 0.002$, $\{(1/b)\Delta g/[1-\gamma M^2+g/b+2t/b]\} = 0.001$, $\{2\Delta t/b/[1-\gamma M^2+g/b+2t/b]\} = 0.001$, $\Delta b/b = 0.015$, and $\Delta M = 0.0$ at $M = 0$ and $\Delta M = 0.01$ at $M = 0.4$. Therefore from Eq. 10, the total uncertainty of the effective wall shear stress $\Delta\tau_{\text{eff}}/\tau_{\text{eff}} = 0.02$ at $M = 0.4$ and 0.015 at $M = 0$. This results in a calibrated uncertainty of $\pm 2\%$ for the chosen MEMS shear stress sensors. The uncertainties from the measurement of Mach number, the gap between the floating element, and the fixed substrate and the thickness of the floating element are negligible and are not considered as a major source of uncertainty. The measurements of the channel height and the pressure gradient are considered to be the largest sources of error and the major contributions to the overall uncertainty of the effective wall shear stress. Because the g and t terms insignificantly affect the uncertainty, then the uncertainty in τ_{eff} is also the uncertainty in τ_w.

V. Results

Two sets of tests are run. In the first the channel is run without a sensor in place. In the second set a sensor is installed, and a calibration run is then implemented.

A. Calibration Channel Test Results

Initial experiments on the flow channel are performed without the shear-stress sensor in place and are aimed at ascertaining the flow channel performance and capabilities. The pressure readings along with the Mach number determinations are compared with the theoretical values for a steady one-dimensional isothermal flow with friction in a constant-area duct, described in Ref. 16. The limiting condition for such a flow in a constant-area duct, choking, is observed with the present calibration flow channel. Variation of Mach number with increase in the flow rate inside the flow channel is shown in Fig. 10. As the flow rate increases, the effective shear stress at the location of the sensor element, calculated using Eq. (7), increases in a monotonic fashion as shown in Fig. 11. The maximum flow rate obtained at a channel height of 230 μm is 43,960 sccm. Further opening of the regulator valve produces no increase in flow rate.

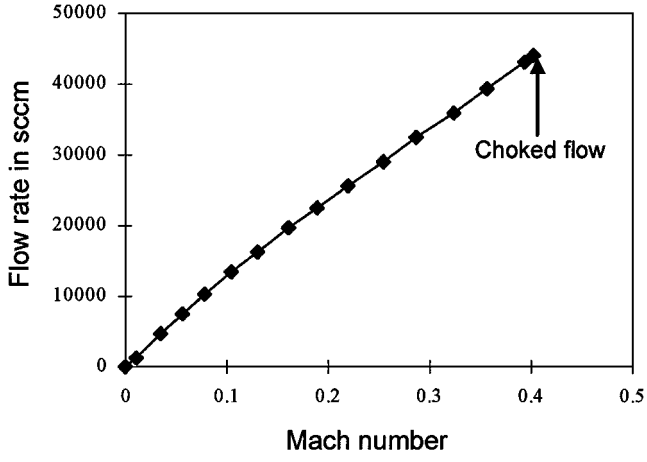

Fig. 10 Mach number at sensor location as a function of flow rate inside the flow channel.

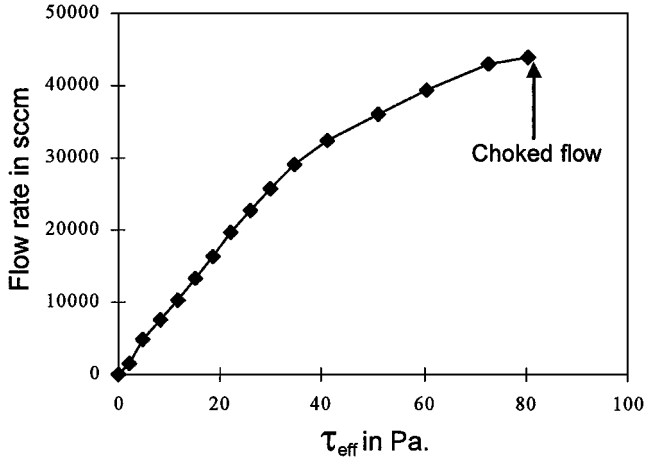

Fig. 11 Effective shear-stress variation with increase in flow rate in the flow channel.

As the gas flows along the flow channel, its static pressure decreases. Eventually a limiting condition, dx/dp equal to zero, is reached where the length of the channel cannot be increased without altering the upstream conditions. The limiting or choking Mach number for steady one-dimensional isothermal flow with friction in a constant-area duct is $M = 1/\sqrt{\gamma}$, which for $\gamma = 1.4$ is $M = 0.845$ at the channel exit. At choking, the effective shear stress at the sensor location is 80.55 Pa, and the Mach number at the sensor location is 0.40.

B. MEMS Shear-Stress Sensor Calibration Results

Typical MEMS shear-stress sensor fabricated at Advanced MicroMachines for Industry (AMMI), a business unit of Rosemount Aerospace, and packaged at Case Western Reserve University are mounted inside the flow channel for calibration. The effective shear-stress values at different flow rates for a fixed channel height are obtained and shear-stress data vs output voltage are plotted. Figures 12 and 13 show the measured output of the multimeter vs the effective shear stress for two different sensors of similar design at the channel heights of 230 and 265 μm, respectively.

In Fig. 13 an irregularity in the curve is observed for a small portion of the plotted data before the response behaves in a linear fashion. This is caused by the stiction effect. The plot shows two regimes with a different sensitivity where the sensor behaves linearly. The sensitivity of the sensor, at 230-μm channel height, in regime I (up to ~25 Pa) is 1.604 mV/Pa and in regime II (beyond 25 Pa) is 0.57 mV/Pa. The linear response for regime I is in the 0.03–0.06-V range and in the 0.065–0.1-V range for regime II. The calibration accuracy is ±2%.

Similar response in the output is observed in a second sensor calibration Fig. 13 for the channel height of 265 μm. The plot of effective shear stress vs output voltage for the calibrated sensor a

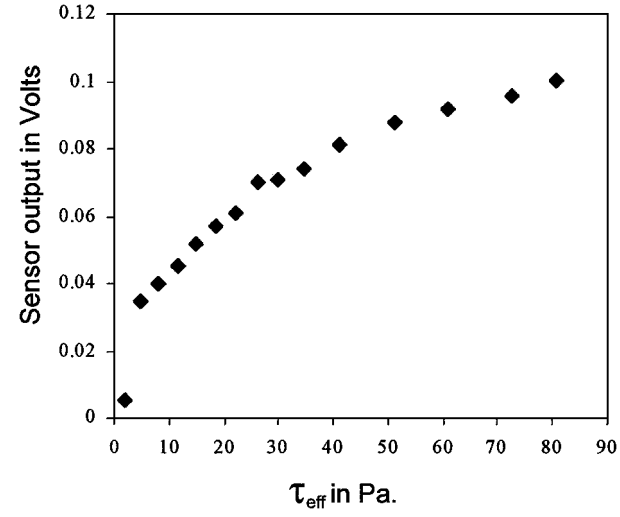

Fig. 12 Typical response of CWRU/analog devices MEMS shear-stress sensor at a channel height of 230 μm (sensor-1).

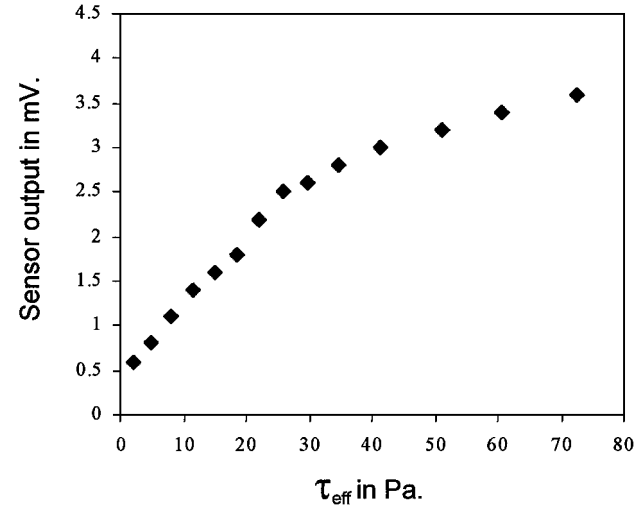

Fig. 13 Typical response of CWRU/analog devices MEMS shear-stress sensor at a channel height of 265 μm (sensor-2).

channel height of 265 μm is shown in Fig. 13. In regime I (up to ~25 Pa) the shear-stress sensor exhibits a sensitivity of about 0.08 mV/Pa in the linear operating range of 0.5 –2.5 mV, whereas in the regime II (beyond 25 Pa) the sensitivity of 0.023 mV/Pa in the linear operating range of 2.5–4 mV is observed. The calibration accuracy again is within 2%.

VI. Discussion

It is interesting to observe the similarity in the transition from regimes I to II in the output of both the sensors that are calibrated. The change in the sensors sensitivity starts when the effective shear-stress value reaches 26 Pa at the sensor location and continues until the value reaches 32 Pa at the sensor location. The sensitivities of both the sensors at different channel heights locations remains constant below the shear stress value of 26 Pa (regime I) and also above 32 Pa (regime II).

The reason behind this change in sensitivity is attributed to the actual floating element design on the sensor chip. In regime I the sensor is operating completely in a forced-balanced mode. The sensor element is in its null position, and the supporting beams are not deflected. In regime II the floating element begins to displace so that part of the restoring force is borne by the beams while the rest by the capacitive restoring force. This explains the reduced sensitivity in regime II. Because both the beam deflection and capacitive restoration are linear, the response in regime II remains linear but with reduced sensitivity.

There is a noticeable jump in the output of Fig. 13 from 0.005 to 0.035 V. This jump is the effect of stiction, a typical problem frequently encountered in the microfabrication of microelectromechanical structures. The microstructure, floating element in the present case, is stuck to the substrate or electrostatic shield immediately beneath the surface. At very low flow rates the shear force produced by the fluid flow is not sufficient to overcome the stictional forces beneath the surface. With the increase in the flow rate, a finite shear force that is required to overcome this stictional force is generated, and the sensor element frees itself from the substrate. Once this has occurred and the shear forces dominate the stiction forces, the floating element deflects in a linear manner.

It has also been observed that the sensor shows photosensitive characteristics. Illumination causes drifts and wavering in the output voltage on the order of several microvolts. Fluctuations in the signal caused primarily by noise, rotameter drift, room illumination, and measurement circuit connections are detected by data-acquisition instruments, and readouts from these instruments are corrected by changing the offset value.

When the flow is initiated at the start of the experiment by opening of the rotameter valve, a transient increase of a few hundred millivolts in the output signal is observed. It has a characteristic decay time of approximately 30–35 s. After the decay the output stabilizes itself to a steady drift, which is then considered as the offset value for the multimeter and is thereupon included as a correction term. This steady drift is considered to be the fixed error for the particular experimental run and is repeatable. Repeatability can be verified by obtaining the same range of the drift after closing and opening the valve of the rotameter.

Saturation of the circuit is obtained at higher shear stresses because the circuit cannot generate strong enough electrostatic forces to counter the shear forces caused by the fluid flow. Saturation level is subject to sensor sensitivity variation, which is inevitable even between mountings and positioning of the same sensor.

The calibration procedure discussed herein results essentially in providing the relationship between the voltage and the total force acting on the sensor element divided by the planform area of the sensor element denoted τ_{eff}. The relationship between τ_{eff} and the wall shear stress τ_w is dependent on pressure gradient and geometry, as indicated in Eqs. (6) and (7). This section discusses the use of a calibrated sensor in a situation where the local pressure gradient is arbitrary.

If the calibration result is described as $\tau_{\text{eff}} = f(V)$, then from Eqs. (6) and (7)

$$\tau_w = f(V) + \frac{\mathrm{d}P}{\mathrm{d}x}\left(\frac{g}{2} + t\right) \tag{11}$$

The pressure gradient in Eq. (11) is the local pressure gradient at the sensor location and must be separately measured, perhaps by a pair of MEMS pressure sensors on the same chip with the shear stress sensor.

In a study done after the completion of this manuscript, Chen and Reshotko[19] did a two-dimensional Navier–Stokes study to determine whether the flow over all parts of the sensor element are subject to the same pressure gradient as is assumed in Eqs. (7) or (11). They found that, because of the low-Reynolds-number character of the flow into and out of the passage beneath the sensor element, the gauge force is higher than assumed, and the shear underneath the sensor element is lower than assumed because of the pressure drops in the passages going into and out of the channel beneath the sensor element. This results in an additional systematic correction to the calibration. For the computed example of Ref. 19,

$$\tau_w = f(V) + \frac{\mathrm{d}P}{\mathrm{d}x}\left(0.932\frac{g}{2} + 1.554t\right) \tag{12}$$

This can change the relation between τ_{eff} and τ_w by up to 1%, depending on the pressure gradient.

VII. Conclusions

A calibration flow channel and a calibration procedure based on continuum isothermal constant-area compressible channel flow have been developed. The calibration channel capabilities have been greatly increased and are now able to sustain shear stresses to 80 Pa. The response of the sensor was studied as a function of flow rate and channel height. A novel microstrip technique is successfully implemented for measuring the channel height, and the reduction in its measurement inaccuracy from ± 20 to ± 3 μm has been obtained. MEMS wall shear-stress sensors incorporating the floating element technique with integrated electronics have been successfully calibrated with an accuracy of $\pm 2\%$.

Acknowledgments

This work was supported by the Air Force Office of Scientific Research under Grant F49620-96-1-0482. The authors thank Mehran Mehregany, the staff of the Microfabrication Laboratory, and Laurie Dudik of Electronics Design Center at Case Western Reserve University for their technical assistance. Special thanks go to Tao Pan of Advanced MicroMachines, BF Goodrich Corp., for providing shear-stress sensors for this research.

References

[1]Pan, T., Hyman, D., Mehregany, M., Reshotko, E., and Garverick, S., "Microfabricated Shear Stress Sensors, Part 1: Design and Fabrication," *AIAA Journal*, Vol. 37, No. 1, 1999, pp. 66–72.

[2]Hyman, D., Pan, T., Reshotko, E., and Mehregany, M., "Microfabricated Shear Stress Sensors, Part 2: Testing and Calibration," *AIAA Journal*, Vol. 37, No. 1, 1999, pp. 73–78.

[3]Alfredsson, P. H., Johansson, A. V., Haritonidis, J. H., and Eckelmann, H., "On the Fluctuating Wall-Shear Stress and Velocity Field in the Viscous Sub-Layer," *Physics of Fluids*, Vol. 31, 1988, pp. 1026–1033.

[4]Preston, J. H., "The Determination of Turbulent Skin Friction by Means of Pitot Tubes," *Journal of the Royal Aeronautical Society*, Vol. 58, 1953, pp. 109–121.

[5]Winter, K. G., "An Outline of the Techniques Available for the Measurement of Skin Friction in Turbulent Boundary Layers," *Progress in Aerospace Sciences*, Vol. 18, 1977, pp. 1–57.

[6]Sheplak, M., Spina, E. F., and McGinley, C. B., "Progress in Hot-Film Anemometry for Hypersonic Flow," *Experimental Thermal and Fluid Science*, Vol. 13, No. 1, 1996, pp. 21–28.

[7]Hyman, D., "Testing and Calibration of Microfabricated Shear Stress Sensors," M.S. Thesis, Dept. of Electrical Engineering and Applied Physics, Case Western Reserve Univ., Cleveland, OH, May 1996.

[8]Pan, T., "Microfabricated Shear Stress Sensors," Ph.D. Dissertation, Dept. of Electrical Engineering and Applied Physics, Case Western Reserve Univ., Cleveland, OH, Jan. 1996.

[9]Schmidt, M. A., Howe, R. T., Senturia, S. D., and Haritonidis, J. H., "Design and Calibration of a Microfabricated Floating-Element Shear-Stress Sensor," *IEEE Transactions on Electron Devices*, Vol. 35, June 1988, pp. 750–757.

[10]Schmidt, M. A., Howe, R. T., Senturia, S. D., and Haritonidis, J. H., "Fabrication and Testing of a Micromachined Shear Sensor," *1987 International Electron Devices Meeting*, Inst. of Electrical and Electronics Engineers, New York, 1987, pp. 282–285.

[11]Schmidt, M. A., "Microsensors for the Measurement of Shear Forces in Turbulent Boundary Layers," Ph.D. Dissertation, Dept. of Electrical Engineering and Computer Science, Massachusetts Inst. of Technology, Cambridge, MA, May 1988.

[12]Pozar, D. M., *Microwave Engineering*, Wiley, New York, 1998, pp. 160–167.

[13]Dudik, Laurie A., and Liu, C. C., "Thick Film Screen Making," *Standard Operating Procedure for Thick Film Screen Making*, Case Western Reserve Univ., Cleveland, OH, June 1996.

[14]Dudik, Laurie A., and Liu, C.C., "Screen Printing on Inks on Substrates," *Standard Operating Procedure for Thick Film Screen Making*, Case Western Reserve Univ., Cleveland, OH, June 1996.

[15]Doeblin, E. O., *Measurement Systems*, 4th ed., McGraw–Hill, New York, 1990, pp. 576, 577.

[16]Zucrow, Maurice J., and Hoffman, Joe D., *Gas Dynamics*, Vol. 1, Wiley, New York, pp. 272–275.

[17]Moffat, R. J., "Describing the Uncertainties in Experimental Results," *Experimental Thermal and Fluid Science*, Vol. 1, 1988, pp. 3–17.

[18]Taylor, J. L., *Computer-Based Data Acquisition Systems: Design Techniques*, Instrument Society of America, Pittsburgh, PA, 1990.

[19]Chen, Y.-R., and Reshotko, E., "Study of Flow Around a MEMS Shear-Stress Sensor Element," *Bulletin of the American Physical Society*, Vol. 46, No. 10, 2001.

R. P. Lucht
Associate Editor